

The effective action in 4-dim CDT. The transfer matrix approach.

J. Ambjørn^{a,b}, J. Gizbert-Studnicki^c, A. Görlich^{a,c}, J. Jurkiewicz^c

^a The Niels Bohr Institute, Copenhagen University
Blegdamsvej 17, DK-2100 Copenhagen Ø, Denmark.
email: ambjorn@nbi.dk

^b IMAPP, Radboud University
Niemegen, The Netherlands,

^c Institute of Physics, Jagellonian University,
Reymonta 4, PL 30-059 Krakow, Poland.
email: jakub.gizbert-studnicki@uj.edu.pl, atg@th.if.uj.edu.pl, jurkiewicz@th.if.uj.edu.pl

Abstract

We measure the effective action in all three phases of 4-dimensional Causal Dynamical Triangulations (CDT) using the transfer matrix method. The transfer matrix is parametrized by the total 3-volume of the CDT universe at a given (discrete) time. We present a simple effective model based on the transfer matrix measured in the de Sitter phase. It allows us to reconstruct the results of full CDT in this phase. We argue that the transfer matrix method is valid not only inside the de Sitter phase ('C') but also in the other two phases. A parametrization of the measured transfer matrix / effective action in the 'A' and 'B' phases is proposed and the relation to phase transitions is explained. We discover a potentially new 'bifurcation' phase separating the de Sitter phase ('C') and the 'collapsed' phase ('B').

1 Introduction

The method of triangulations was introduced in the context of General Relativity by Regge [1] to discretize the continuous Hilbert-Einstein action

$$S_{HE}[g] = \frac{1}{16\pi G} \int d^4x \sqrt{-g} (R - 2\Lambda). \quad (1)$$

Continuous geometries are approximated by piecewise linear simplicial manifolds. The curvature is represented as a (discrete) deficit angle concentrated at the (D-2) subsimplex. A particular realization of this idea is the method of Dynamical Triangulations (DT), where the piecewise linear simplicial manifolds are built by gluing together regular, identical simplices with identical edge lengths a [2]. The DT set of simplicial geometries is thus entirely characterized by the abstract triangulations which define how the simplices are glued together and it has been useful in Monte Carlo simulations of quantum gravity, a acting as a UV cut off. In D=2 one could even solve the DT model analytically for gravity coupled to certain simple matter systems and the continuum limit $a \rightarrow 0$ could be obtained. These results were reproduced by conformal field theory methods (so-called 2D quantum Liouville theory) [3].

For higher dimensional quantum gravity the DT approach has been less successful [4, 5]. Firstly, there are only very few analytical results. Most investigations use Monte Carlo simulations to evaluate the path integrals. This method has also been tested and has proven very successful in $D = 2$. Secondly, in the three- and four-dimensional DT cases the simplest versions of the lattice theory, characterized by two coupling constants, analogous to that of the continuum theory (1), did not show a behavior which could be viewed as interesting from a continuum gravity point of view. Depending on the strength of the bare lattice gravitational coupling constant, the system (rotated to Euclidean time in order to allow for Monte Carlo simulations) appeared to have two phases. The weak gravity phase was dominated by the branched polymer geometries with a Hausdorff dimension $d_H = 2$ and the strong gravity phase by collapsed geometries with $d_H = \infty$, corresponding to universes without the linear extension. The two phases were separated by the first order phase transition [6].

The method of Causal Dynamical Triangulations (CDT) was introduced to cure these problems [7] (for pedagogical reviews see [8]). At this point it should be made clear that the problems encountered in DT could very well reflect the fact that there *is* no stand alone theory of quantum gravity based only on the metric tensor $g_{\mu\nu}$. This is in a certain way what we are trying to investigate. CDT enlarges the scope of metric theories one can reach, but eventually one might encounter some of the same problems as in DT. In CDT a notion of the proper time was introduced together with the requirement that the spatial topology of the quantum universe with respect to this proper time must be preserved in the time evolution [9]. The simplest version of the discretized theory using the CDT approach has three parameters. Apart from the two parameters present in the DT approach, related to the cosmological constant and to the gravitational constant, the additional parameter controls a possible asymmetry between the edge lengths in the spatial and time directions. In numerical simulations the topology of the manifold is assumed to be $S_3 \times S_1$ with periodic boundary conditions in the

(Euclidean) time. This choice was dictated by practical reasons. Geometric structures used to build simplicial manifolds of CDT are characterized by their position in spatial and time directions. In particular we use two types of four-simplices: $\{4, 1\}$ with four vertices at time t and one at $t \pm 1$ and $\{3, 2\}$ with three vertices at t and two at $t \pm 1$. All simplices of a particular type are assumed to have the same sizes. The discretized Regge action in this case takes a form [8]:

$$S_R = -(K_0 + 6\Delta)N_0 + K_4 (N^{\{4,1\}} + N^{\{3,2\}}) + \Delta N^{\{4,1\}} \quad (2)$$

where: N_0 is the total number of vertices in the triangulation, $N^{\{4,1\}}$ and $N^{\{3,2\}}$ are the total numbers of simplices of two different types, K_0 , K_4 and Δ are the (bare) dimensionless coupling constants obtained by the discretization of the continuous action (1). An additional geometric parameter is the length t_{tot} of the periodic time axis.

In numerical simulations the total four-volume of the universe is kept fixed. In practice this restricts the number $N^{\{4,1\}}$ to fluctuate around a fixed value \bar{N}_{41} . For a fixed space-time topology the number of CDT triangulations with \bar{N}_{41} $\{4, 1\}$ simplices grows exponentially with \bar{N}_{41} . This exponential growth determines critical value of the bare lattice cosmological constant K_4 . Requiring the average $\langle N^{\{4,1\}} \rangle$ to be fixed is equivalent with fixing the bare cosmological constant K_4 to be close to the critical value K_4^{crit} . For $K_4 < K_4^{crit}$ the *partition function*

$$\mathcal{Z} = \sum_{\mathcal{T}} e^{-S_R} \quad (3)$$

becomes divergent.

The remaining two bare coupling constants can be freely adjusted and characterize the physical content of the theory. Numerical simulations proved that depending on these values the quantum system can be in three different phases [10]. From a physical point of view the most interesting is the *de Sitter phase*, where a typical geometry can be viewed as a quantum fluctuation around a semi-classical regular four-sphere, or rather four-ellipsoid with different scale in time and spatial directions [11]. A natural quantity used to parametrize the configurations is the distribution n_t of $\{4, 1\}$ volumes as a function of the discrete time t . n_t is closely related to the scale factor in the mini-superspace approach to quantum gravity. n_t is equal to twice the number of three-dimensional tetrahedra which form a spatial slice (with S^3 topology) at time t . This is because each spatial tetrahedron located in time-slice t is shared by precisely two $\{4, 1\}$ four-simplices, one with a vertex at time-slice $t + 1$ and one with a vertex at time-slice $t - 1$ (and of course four vertices at time-slice t). In de Sitter phase the distribution of n_t has a characteristic shape (Fig. 1), consisting of the *blob* which fluctuates around a four-sphere and a *stalk* with an almost minimal size, which is present

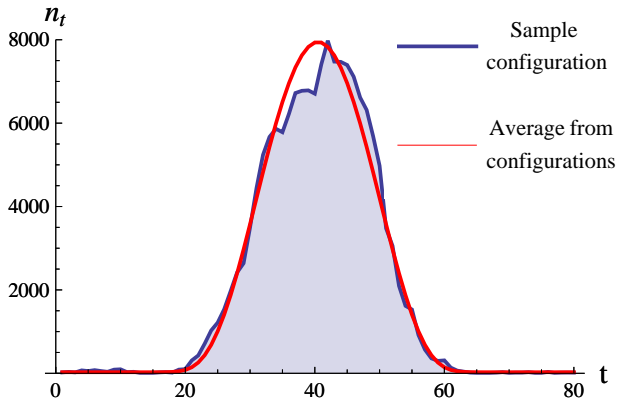


Figure 1: Distribution n_t of a $\{4,1\}$ volume inside de Sitter phase. Data for $K_0 = 2.2$, $\Delta = 0.6$ for an individual configuration (blue line) and an average distribution (red line).

because the global topology $S_3 \times S_1$ is not allowed to be broken in the computer simulations. The distribution of spatial volume can be averaged over many configurations obtained in the numerical simulations. In the blob the average spatial volume profile $\langle n_t \rangle \propto \cos^3(t/B)$ which corresponds to a (Wick rotated) de Sitter solution of Einstein's equations. Fluctuations around this semi-classical trajectory $\Delta n_t = n_t - \langle n_t \rangle$ are correlated for different t . The covariance matrix of fluctuations can be measured. The inverse of the covariance matrix can be used to determine the *effective action* in terms of n_t [12, 8]. It was shown in [13] that it corresponds to a naively discretized mini-superspace action.

$$S_{eff}^{blob} = \frac{1}{\Gamma} \sum_t \left(\frac{(n_t - n_{t+1})^2}{n_t + n_{t+1}} - \lambda n_t + \mu n_t^{1/3} + \mathcal{O}(n_t^{-1/3}) \right) \quad (4)$$

where Γ is proportional to the effective Newton's constant while the effective cosmological constant λ together with the parameter μ fix the total 4-volume of the universe.

This form of the action leads in a natural way to the path-integral representation with the weight $\exp(-S_{eff})$ of each configuration given by a product

$$\exp(-S_{eff}) \equiv \prod_t \exp(-L_{eff}(n_t, n_{t+1})) \quad (5)$$

of pseudo-local transfer matrix

$$\langle n_t | M | n_{t+1} \rangle \propto \exp(-L_{eff}(n_t, n_{t+1})) \quad (6)$$

linking the nearest (in time) spatial slices. In this form all details of the geometric structure space at a given slice are wiped out and we assume that it makes sense to use the *effective* quantum states $|n_t\rangle$ with unit norm as the eigenstate basis at each slice.

The transfer matrix can be measured in numerical simulations. In [14] we used this concept to determine the form of the effective action inside the de Sitter phase. We found that the symmetrized form of (4) with minor small-volume correction fits very well to our numerical data both in the blob and the stalk range of the CDT universe. This result was obtained in numerical simulations of systems with small time extension ($t_{tot} = 2, 3, 4$).

In CDT there exists a “genuine” transfer matrix M_{gen} connecting states at time t and time $t + 1$. These states can be chosen as the states of spatial geometries, and in this simplicial approach a given spatial geometry is completely characterized by the corresponding DT triangulation of S^3 (which is part of the 4d CDT triangulation). Thus we have by definition for the “genuine” transfer matrix:

$$\begin{aligned} & \langle T(t+n) | M_{gen}^n | T(t) \rangle = & (7) \\ & = \sum_{T(t+i), 1 < i < n-1} \langle T(t+n) | M_{gen} | T(t+(n-1)) \rangle \cdots \langle T(t+1) | M_{gen} | T(t) \rangle \end{aligned}$$

The number of states $|T(t)\rangle$ is of course much larger than the number of so-called “effective” quantum states $|n_t\rangle$ mentioned above. The claim that the effective transfer matrix describes CDT well contains two aspects, namely

$$\langle T(t+1) | M_{gen} | T(t) \rangle \sim \langle n_{t+1} | M | n_t \rangle, \quad (8)$$

for generic states $|T\rangle$, as long as we only measure n_t , and even stronger

$$\langle T(t+n) | M_{gen}^n | T(t) \rangle \sim \langle n_{t+n} | M^n | n_t \rangle, \quad (9)$$

again when we only look at n_t . To be reassured that the effective transfer matrix approach is correct we have to check (9) for large n , that is for systems where $t_{tot} \gg 1$. The aim is to reproduce the full CDT results (the volume profile $\langle n_t \rangle$ and quantum fluctuations Δn_t) by studying the simplified effective model based on the measured transfer matrix.

We also want to extend our analysis of the effective transfer matrix / action to two other phases of CDT which are the analogues of the branched polymer and collapsed phases of DT. This is especially interesting in the context of phase transitions. Recent results [15] showed that the phase transition between de Sitter and collapsed phase is second (or higher) order which makes it a natural candidate in the quest for UV fixed point of CDT. Therefore it would be tempting to better understand the mechanism of the phase transitions from a microscopic perspective.

2 Methodology of the transfer matrix measurement

To investigate the properties of CDT in four dimensions we perform computer simulations of systems with (time) periodic boundary conditions and S^3 spatial topology. The action used in computer simulations is the Regge discretization of the Einstein-Hilbert action (2).

Studies of the covariance matrix of spatial volume fluctuations

$$C_{tt'} \equiv \langle (n_t - \langle n_t \rangle)(n_{t'} - \langle n_{t'} \rangle) \rangle$$

suggest that the effective action couples only adjacent time slices and that there exists an effective transfer matrix, namely the one defined in (6).

Inside the de Sitter phase the measurement and parametrization of the transfer matrix is straightforward. In the other two phases it has to be done with some care. The most problematic phase is the ('time collapsed') phase 'B', in which time translation symmetry is strongly broken in generic triangulations.

Measurements inside this phase required updating the Monte Carlo code used in computer simulations. The new measurement method uses a system with just two time slices and one has to avoid artificial repetition of (sub)simplices (the problem does not occur for time extension above two time slices). We checked that inside de Sitter phase the results of the new method are fully consistent with the previous one (based on the systems with 3 and 4 time slices).

In order to measure the transfer matrix we need systems with a small time period t_{tot} . In our transfer matrix parametrization the probability to measure the combination of 3-volumes $n_t = N^{\{4,1\}}(t)$ in times $t = 1 \dots t_{tot}$ is given by:

$$P^{(t_{tot})}(n_1, n_2, \dots, n_{t_{tot}}) = \frac{\langle n_1 | M | n_2 \rangle \langle n_2 | M | n_3 \rangle \dots \langle n_{t_{tot}} | M | n_1 \rangle}{\text{tr } M^{t_{tot}}} \quad (10)$$

In a system with two time slices ($t_{tot} = 2$) we have:

$$P^{(2)}(n_1, n_2) = \frac{\langle n_1 | M | n_2 \rangle \langle n_2 | M | n_1 \rangle}{\text{tr } M^2}$$

which implies:

$$\langle n | M | m \rangle \propto \sqrt{P^{(2)}(n_1 = n, n_2 = m)} \quad (11)$$

where we use the assumption that due to time-reflection symmetry the transfer matrix is also symmetric.

We can as well use the probability distributions measured in Monte Carlo simulations with $t_{tot} = 3$ and 4 (this was done in our earlier investigations). In

this approach the transfer matrix elements can be computed as

$$\langle n|M|m\rangle \propto \frac{P^{(3)}(n_1 = n, n_2 = m)}{\sqrt{P^{(4)}(n_1 = n, n_3 = m)}} \quad (12)$$

We checked that both approaches agree inside the de Sitter phase 'C'.

The advantage of the new method with $t_{tot} = 2$ is twofold. First of all one needs only to measure a single probability distribution, thus leading to a reduction of computer time and a diminishing of statistical errors (since one does not need to combine two probability measurements like in (12)). However, more importantly, by an appropriate choice of volume fixing (see below) one can measure off-diagonal elements of the transfer matrix with much higher precision. It is especially important when extracting the kinetic part of the effective action in the 'A' and 'B' phases.

To perform the computer simulations efficiently one has to introduce some kind of volume fixing. This is done by adding to the usual Regge action (2) an additional volume fixing term:

$$S_R \rightarrow S_R + S_{VF}$$

In our simulations with $t_{tot} = 2$ we use the global volume fixing¹ either with a quadratic or a linear potential:

$$S_{VF} = \epsilon(n_1 + n_2 - n_{vol})^2 \quad \text{or} \quad S_{VF} = \epsilon|n_1 + n_2 - n_{vol}| \quad (13)$$

The effect of the volume fixing term can be easily removed from the measured transfer matrix \widetilde{M} defined by (11) by setting:

$$\langle n|M|m\rangle = e^{\frac{1}{2}\epsilon(n+m-n_{vol})^2} \langle n|\widetilde{M}|m\rangle \quad \text{or} \quad \langle n|M|m\rangle = e^{\frac{1}{2}\epsilon|n+m-n_{vol}|} \langle n|\widetilde{M}|m\rangle \quad (14)$$

for a quadratic or a linear volume fixing, respectively.

The volume fixing correction (14) clearly affects the diagonal elements of the transfer matrix used in the analysis of the the potential term (see below) whereas the cross-diagonal elements, important to determine the kinetic term, are simply rescaled for $n + m = const.$

¹Our previous approach used (12) based on probability distributions measured in systems with $t_{tot} = 3, 4$, and we used a *local* volume fixing procedure (see [14] for details). The transfer matrix measurement with global volume fixing is possible only with $t_{tot} = 2$ and is especially suitable in the 'A' and 'B' phases where generic configurations typically have very different spatial volumes on neighboring time slices.

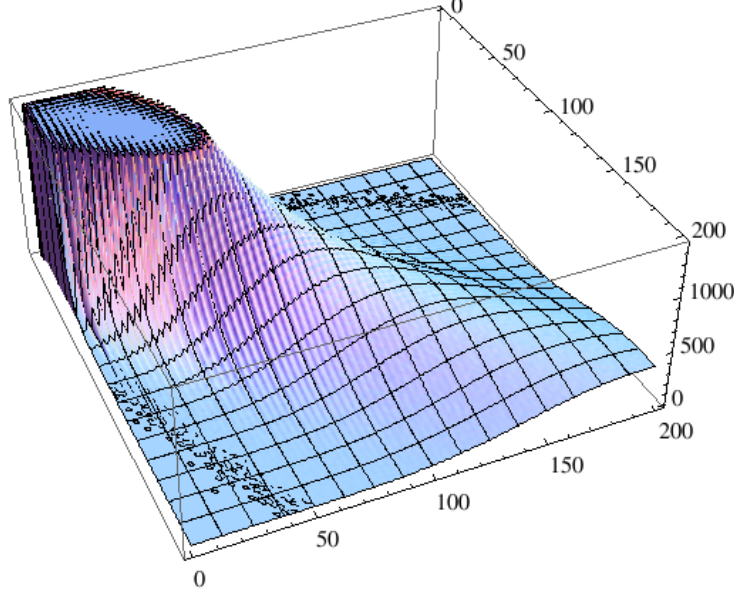


Figure 2: Measured transfer matrix elements $\langle n|M|m\rangle$ in the de Sitter phase 'C'. For small values of n and m we observe strong discretization effects. For larger volumes the behavior is smooth.

3 The effective model in the de Sitter phase

Recent results show that for small t_{tot} the measured transfer matrix in the de Sitter phase does not depend on the number of slices supporting the decomposition (10). An example of the measured transfer matrix is plotted in Fig. 2.

In order to reconstruct the results of the full CDT simulations we will need matrix elements $M_{nm} \equiv \langle n|M|m\rangle$ for large volumes n, m . As can be seen from Fig. 3, for a total four-volume with $\bar{N}_{41} = 40k$ the largest spatial volumes n_t reach values above 3000. Technically it is difficult to measure matrix elements in such wide range, but we can use extrapolation for large volumes.

For small volumes the transfer matrix elements are dominated by very strong discretization effects as can be seen in Fig. 2, but as n and m increase the behavior becomes much smoother. For sufficiently large large spatial volumes the transfer matrix is very well described by the effective Lagrangian introduced in [14],

$$L_{eff}(n, m) = \tag{15}$$

$$= \frac{1}{\Gamma} \left[\frac{(n-m)^2}{n+m-2n_0} + \mu \left(\frac{n+m}{2} \right)^{1/3} - \lambda \left(\frac{n+m}{2} \right) - \delta \left(\frac{n+m}{2} \right)^{-\rho} \right].$$

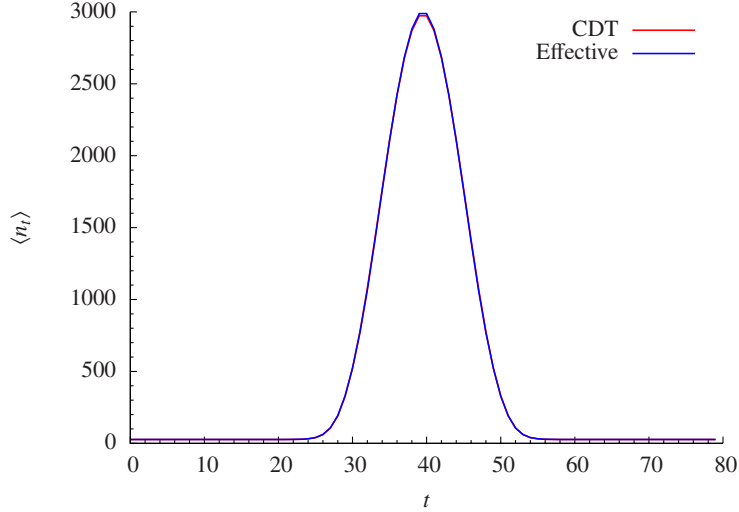


Figure 3: The average volume profile $\langle n_t \rangle$ for full CDT in the de Sitter phase (red) and the effective model (blue) for $t_{tot} = 80$ and $\bar{N}_{41} = 40k$.

We use the measured (empirical) transfer matrix $M_{nm}^{(\text{emp})}$, $250 < n, m < 700$, to determine the parameters $\Gamma, n_0, \mu, \lambda, \delta$ and ρ , by making a best fit of

$$M_{nm}^{(\text{th})} = \mathcal{N} e^{-L_{eff}(n,m)}. \quad (16)$$

to $M_{nm}^{(\text{emp})}$. For larger values of n, m we then use $M_{nm}^{(\text{th})}$ with $L_{eff}(n, m)$ determined by this fit.

Finally, we thus define the semi-empirical transfer matrix by

$$M_{nm} = \begin{cases} M_{nm}^{(\text{emp})} & n < thr \text{ or } m < thr, \\ M_{nm}^{(\text{th})} & \text{otherwise.} \end{cases} \quad (17)$$

where thr is a threshold ($thr = 300$). When one of the entries is smaller than the threshold we use directly measured elements. When both entries are larger than the threshold we use the extrapolating function (16). Fig. 4 presents the diagonal $\langle n|M|n \rangle$ (left) and an anti-diagonal $\langle n|M|s-n \rangle$ (right) of the semi-empirical transfer matrix. The blue points denote the empirical part of M , used for volumes below threshold, $n < 300$ or $m < 300$. The red line presents a theoretical fit of the form (16), the fitting range being $250 - 700$. The green points correspond to the theoretical part of M given by (16) for volumes above threshold, $n, m > 300$. The agreement between the empirical transfer matrix and the fit plotted with red line is very good also below $n = 250$ but gets even better above the threshold. The extrapolation (16) allows us to expand the transfer matrix to volumes which are

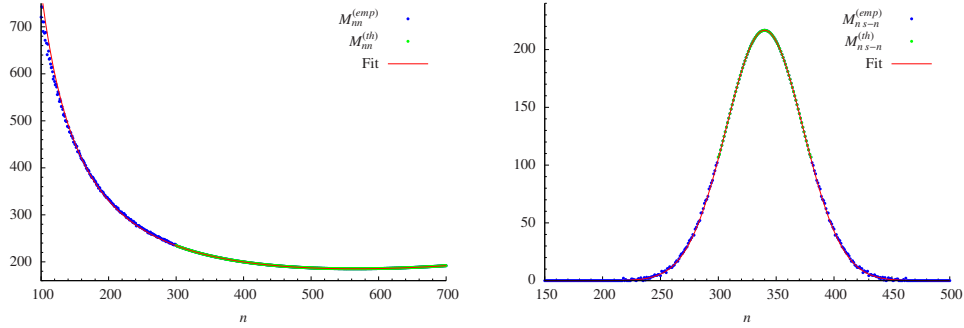


Figure 4: The effective transfer matrix in de Sitter phase merged from the empirical matrix (blue) and theoretical part (green) based on the best fit (red line). Left: Diagonal $\langle n|M|n \rangle$. Right: Anti-diagonal $\langle n|M|s-n \rangle$, $s = 680$.

not easily accessible in direct measurement. Nevertheless, because the effective Lagrangian describes perfectly the measured transfer matrix in the range where we can make the comparison, and seemingly gets better the larger are the values of the entries (n, m) , this extrapolation beyond actual empirical data should not be of any importance when judging the validity of the effective transfer matrix decomposition (10).

We now introduce an effective model which aims to reproduce results of the full CDT model in the de Sitter phase. In this approach configurations are given by volume profiles $\{n_t\}$ rather than by triangulations \mathcal{T} . The model is based on the effective transfer matrix decomposition (10) with the usual total volume fixing term used in the full CDT simulations:

$$P(n_1, \dots, n_{t_{tot}}) \propto \langle n_1|M|n_2 \rangle \langle n_2|M|n_3 \rangle \cdots \langle n_{t_{tot}}|M|n_1 \rangle e^{-\epsilon(\sum_t n_t - \bar{N}_{41})^2} \quad (18)$$

We can specify the probability distribution of configurations using the transfer matrix $\langle n|M|m \rangle$ constructed in (17). In order to recover results of the original model we have to access matrix elements for large volumes.

Next, we apply standard Monte Carlo methods to generate the configurations, i.e. t_{tot} -component vectors $\{n_t, t = 1 \dots t_{tot}\}$, according to the volume distributions (18). We use the same number of slices t_{tot} and total volume \bar{N}_{41} as in the full CDT simulations. As before, we measure the average volume profile $\langle n_t \rangle$ and the covariance matrix $C_{tt'} \equiv \langle (n_t - \langle n_t \rangle)(n_{t'} - \langle n_{t'} \rangle) \rangle$. Surprisingly, the results obtained with this effective model are to a high degree identical with results obtained with the original, full CDT model. Fig. 3 shows the average volume profile $\langle n_t \rangle$ measured in the full CDT simulations (the red line) and in the reduced model simulations (the blue line). The two curves overlap almost exactly. The diagonal

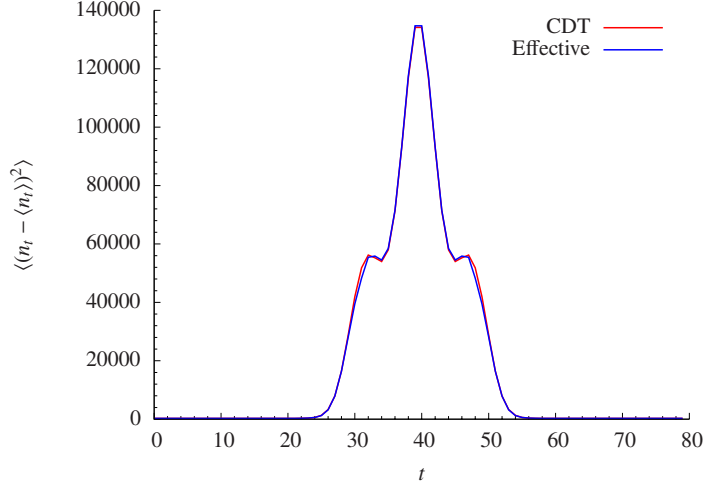


Figure 5: Variance of spatial volumes $\langle (n_t - \langle n_t \rangle)^2 \rangle$ for full CDT in de Sitter phase (red line) and the effective model (blue line). It corresponds to the diagonal of the covariance matrix $C_{tt'}$.

of the covariance matrix C_{tt} , i.e. variance of n_t , is shown in Fig. 5. Again, results of the original, full CDT model (the red line) and of the effective model (the blue line) are in complete agreement.

4 Extracting the kinetic and potential terms

The transfer matrix measured in computer simulations can be used to determine the form of the effective action / Lagrangian. It was shown in [14] that in the de Sitter phase 'C' the action is very well approximated by a simple discretization of the continuum minisuperspace action with a minor small-volume correction, more precisely by the $L_{eff}(m, n)$ given in (15). The form of the discretization suggests that the transfer matrix can be factorized into potential and kinetic parts:

$$\langle n|M|m \rangle = \mathcal{N} \underbrace{\exp\left(-v[n+m]\right)}_{potential} \underbrace{\exp\left(-\frac{(n-m)^2}{k[n+m]}\right)}_{kinetic} \quad (19)$$

where the functions:

$$v[n+m] = \frac{\mu}{\Gamma} \left(\frac{n+m}{2}\right)^{1/3} - \frac{\lambda}{\Gamma} \left(\frac{n+m}{2}\right) - \frac{\delta}{\Gamma} \left(\frac{n+m}{2}\right)^{-\rho} \quad (20)$$

$$k[n+m] = \Gamma \cdot (n+m-2n_0) \quad (21)$$

will be called the potential and kinetic coefficients, respectively.

The **potential** part can be easily analyzed by looking at the **diagonal** elements of the transfer matrix:

$$v[2n] = -\log \langle n|M|n \rangle + \log \mathcal{N} \quad (22)$$

while the **kinetic** term requires extracting the **cross-diagonal** elements:

$$\langle n|M|s-n \rangle = \mathcal{N}(s) \exp\left(-\frac{(2n-s)^2}{k[s]}\right) \quad (23)$$

By measuring potential coefficients for different n and kinetic coefficients for different s one may verify that indeed equations (20) and (21) hold in de Sitter phase [14].

We will apply the same factorization to analyze the measured transfer matrices in phases 'A' and 'B'. Further, we will check how the kinetic and potential terms change when we move between phase 'A' and 'C' as well as between phase 'B' and 'C'.

5 The transfer matrix in phase 'A'

We measured the transfer matrix in a generic point inside phase 'A' ($K_0 = 5.0, \Delta = 0.4, K_4 = 1.22$) using the method described in Section 2 with $t_{tot} = 2$ and a quadratic volume fixing term.

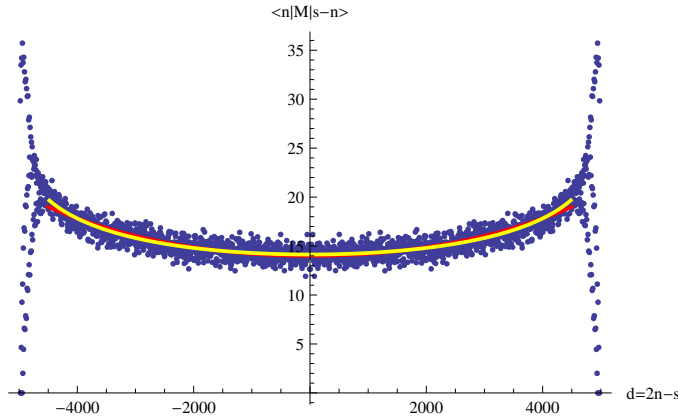


Figure 6: Sample cross-diagonal of the measured transfer matrix inside phase 'A' ($K_0 = 5.0, \Delta = 0.4, K_4 = 1.22$). The data are for $s=n+m=5000$. The red line corresponds to the fit of the 'artificial' "anti-Gaussian" (24) whereas the yellow line is the fit function in the effective Lagrangian (29).

The kinetic part can be analyzed by looking at cross-diagonal elements of the transfer matrix: $\langle n|M|m \rangle = \langle n|M|s - n \rangle$. The generic shape of the measured cross-diagonal is presented in Fig. 6 where $\langle n|M|m \rangle$ is plotted as a function of $(n - m) = d$. The shape looks very different from the typical behavior in phase 'C' (where it is Gaussian, cf. Fig. 4). Disregarding strong discretization artifacts for small volumes one could naively say that the cross-diagonals of the measured transfer matrix can be fitted with a very flat “anti-Gaussian” function. Indeed we tried to fit (red line in Fig. 6):

$$\langle n|M|s - n \rangle = \mathcal{N}(s) \exp\left(\frac{d^2}{k[s]}\right) \quad (24)$$

The kinetic coefficient $k[s]$ as a function of s is presented in Figure 7. In contrast

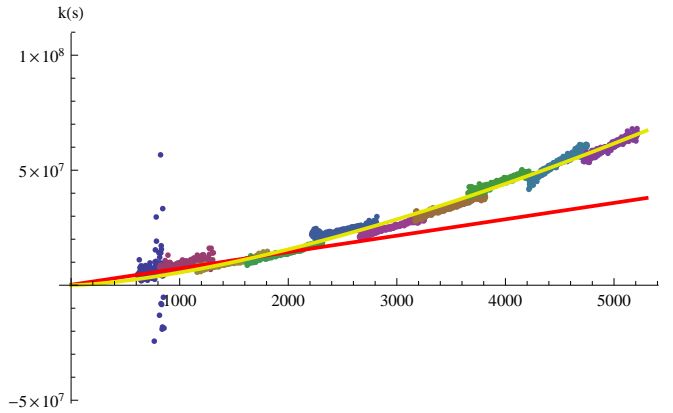


Figure 7: The kinetic coefficient $k[s]$ measured in phase 'A' ($K_0 = 5.0, \Delta = 0.4, K_4 = 1.22$). $k[s]$ is not linear (red line) but can be fitted with eq. (25) (yellow line).

to the behavior in phase 'C', $k[s]$ is no longer linear. It can be fitted with the following parametrization (yellow curve in Fig. 7):

$$k[s] = k_0 s^{2-\alpha} \quad (25)$$

The best fit is for $\alpha = 0.50 \pm 0.01$ and $k_0 = 175 \pm 10$.

The anti-Gaussian behavior of the kinetic part is somehow strange. Covariance analysis of triangulations in phase 'A' shows that the volume distributions in different time slices are not correlated. Therefore the kinetic part should vanish and what we observe can be just an artifact of the measurement / parametrization method.

Let us assume that in phase 'A' 3-volume distributions in different time slices are independent and some local potential exists. This naturally leads to an effec-

tive Lagrangian of the form:

$$L_A(n, m) = \mu (n^\alpha + m^\alpha) - \lambda(n + m) \quad (26)$$

One can change this parametrization to: $s = n + m$, $d = n - m$ and assume d/s small:²

$$\begin{aligned} L_A(n, m) &= \mu \left(\frac{s}{2}\right)^\alpha \left[\left(1 + \frac{d}{s}\right)^\alpha + \left(1 - \frac{d}{s}\right)^\alpha \right] - \lambda s = \\ &= -\lambda s + \mu \left(\frac{s}{2}\right)^\alpha \left[2 + \alpha(\alpha - 1) \left(\frac{d}{s}\right)^2 \right] + \mathcal{O}(d^4) \end{aligned} \quad (27)$$

For $\alpha < 1$ we effectively get an “anti-Gaussian” behavior of the transfer matrix cross-diagonals (24) with:

$$k[s] = \frac{2^\alpha}{\mu \alpha (1 - \alpha)} s^{2-\alpha} \quad (28)$$

exactly in line with our measurements (25). From the fitted values of α and k_0 one can calculate $\mu = 0.032 \pm 0.002$.

As a check of parametrization (26) one may use the effective Lagrangian L_A to fit cross-diagonal elements of the measured transfer matrix:

$$\langle n|M|s-n \rangle = \mathcal{N} \exp[-L_A(n, s-n)] = \mathcal{N}(s) \exp[-\mu n^\alpha - \mu(s-n)^\alpha] \quad (29)$$

The best fit for $\alpha = 0.5$ is presented as a yellow curve in Fig. 6 and gives $\mu = 0.022 \pm 0.001$. The parameter μ fitted for different cross-diagonals (as a function of s) is presented in Figure 8. The value of μ tends to a constant for large volumes (big s) as discretization effects get smaller. The red line corresponds to $\mu = 0.024$.

The analysis of the potential part is now straightforward:

$$\log \langle n|M|n \rangle = -L_A(n, n) + \log \mathcal{N} = -2\mu n^\alpha + 2\lambda n + \log \mathcal{N} \quad (30)$$

The diagonal elements of the measured transfer ed matrix together with the best fit of $\mu = 0.026$ (for $\alpha = 0.5$) are presented in Figure 9.

As a side remark we may go back to the analysis of the de Sitter phase ‘C’. In this phase we use the parametrization (15) with symmetrized potential terms. As a result the potential coefficient is a function of the sum of volumes in the adjacent time slices ($v[n+m]$). If instead the true potential was not symmetric (a function of n and m separately) one should expect the same kind of effective “anti-Gaussian” term to appear. However this effect is very small compared to the generic Gaussian behavior of the kinetic part. As a result the kinetic coefficients $k[n+m]$ would be slightly modified, which may explain the existence of the non-vanishing but very small n_0 in the measured effective Lagrangian (15).

²For cross-diagonal terms it is not always true as d/s can be of order 1 and higher order corrections should be taken into account.

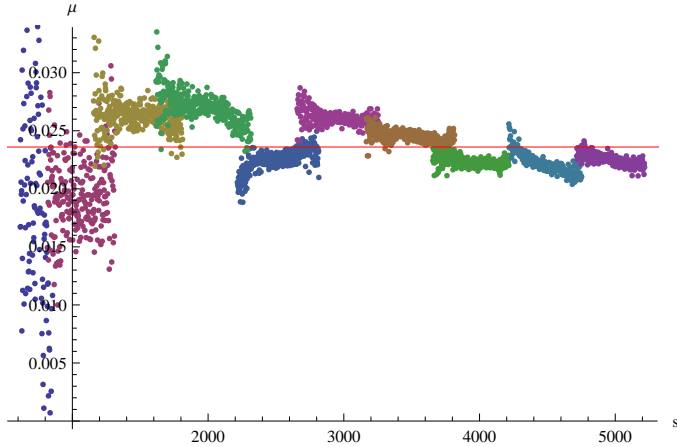


Figure 8: μ as a function of s measured in phase 'A' ($K_0 = 5.0, \Delta = 0.4, K_4 = 1.22$). The value of μ stabilizes around 0.024 (the red line) as the discretization effects vanish.

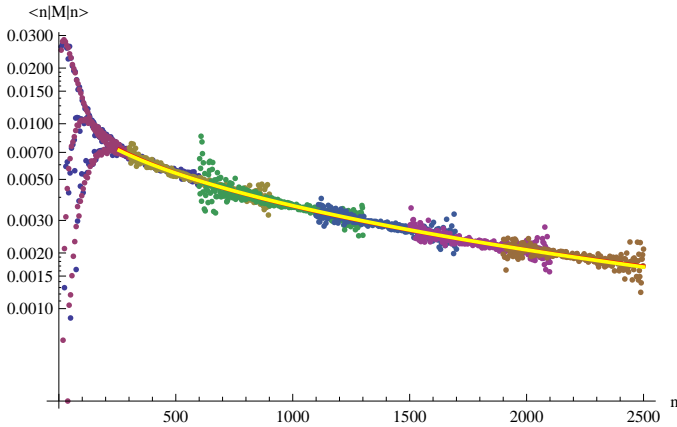


Figure 9: The diagonal elements of the transfer matrix measured in phase 'A' ($K_0 = 5.0, \Delta = 0.4, K_4 = 1.22$) shown together with the best fit to eq. (30). The fit disregards strong discretization effects visible for small volumes.

6 The transfer matrix in phase 'B'

The analysis of the transfer matrix in phase 'B' is not straightforward. Generic triangulations in this phase are 'collapsed' i.e. the spatial 3-simplices of almost all $\{4, 1\}$ simplices (i.e. the spatial volume) are concentrated in a single time slice. As a result we do not have much information about volume-volume correlations.

As an additional issue the potential part of the effective action inside phase 'B' seems to suffer from a strong non-linear dependence on the total volume s in the small to medium volume regime. In our simulations we fix the K_0 and

Δ coupling constants of the Regge action (2), while K_4 (which is conjugate to the total volume in the triangulation) is fine-tuned to offset the spontaneously emerging entropic / potential term coming from the exponentially large number of configurations with constant total volume s . If the emerging effective potential is linear (this is the exponentially growing number of configurations with s) the value of K_4 is constant. The non-linear corrections reflect subleading corrections to the exponentially growing number of configurations. They might be small power-like corrections which can effectively be neglected. Our simulations show that corrections to K_4 due to non-linear components in the effective action (15) in phase 'C' and in the effective action (26) in phase 'A' indeed are negligible, even in the small volume region (they change the fourth significant digit which is of the same order as the accuracy of the K_4 fine-tuning). The situation is much different in the 'B' phase where the value of K_4 is strongly volume dependent even for relatively large volumes. It is illustrated in Fig. 10, where the value of K_4 is plotted as a function of total volume s together with the fit:

$$K_4(s) = K_4^\infty - \beta s^{-\gamma} \quad (31)$$

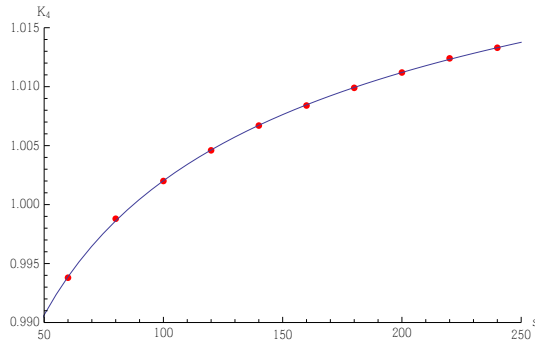


Figure 10: K_4 scaling with total volume (s in '000) inside phase 'B' (for $K_0 = 2.2, \Delta = 0.0$) and the best fit of (31).

The strong volume dependence of K_4 on s implies that it is technically impossible to measure the transfer matrix in phase 'B' for the values of K_4 appropriate for large volume limit. If we fix the K_4 value to the critical value corresponding to a large volume, effectively this value is “too large” and the system will oscillate around the minimally allowed configuration and only very seldom make detours to the large values of s corresponding to the chosen value of K_4 . To circumvent this problem we decided to use lower values of K_4 and analyze how a change of K_4 affects the measured transfer matrix. As a result we can (at least qualitatively) estimate the properties of the transfer matrix in the continuum limit.

In this section we present the results for measurement performed at a generic point in phase 'B' ($K_0 = 2.2$ and $\Delta = 0.0$). We start our analysis with the

transfer matrix measured for $K_4 = 0.943$ using $t_{tot} = 2$ with quadratic total volume fixing. We explicitly symmetrize the data: $\langle n|M|m \rangle = \langle m|M|n \rangle$ even though the measured probabilities of volume distributions are highly asymmetric in general. This is equivalent to regaining the time-reflection symmetry of the transfer matrix which is strongly broken by generic configurations.

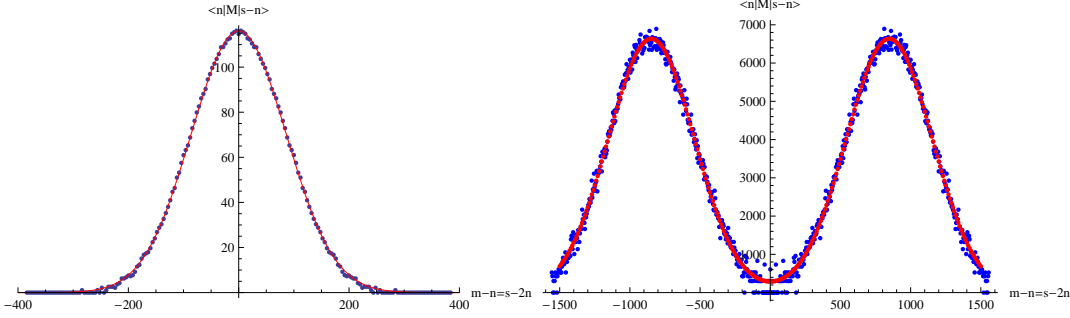


Figure 11: Cross diagonals of the transfer matrix measured in phase 'B' (for $K_0 = 2.2$, $\Delta = 0.0$ and $K_4 = 0.943$). The left chart shows the data below bifurcation point ($s = n + m < s^b$). The right chart presents cross-diagonals above bifurcation point ($s > s^b$). The best fits of eq. (32) are presented as red lines.

The typical behavior of the cross-diagonal (kinetic) part of the measured transfer matrix $\langle n|M|m \rangle = \langle n|M|s - n \rangle$ strongly depends on $s = n + m$. For $s < s^b$ it looks the same as in phase 'C' and can be well fitted with a single Gaussian (23) - see Figure 11 (left). For $s > s^b$ the cross-diagonals split into the sum of two "shifted" Gaussians - see Figure 11 (right). The value of the shift depends on $s = n + m$ (Figure 12). All together the kinetic part can be parametrized by:

$$\begin{aligned} \langle n|M|m \rangle &= \langle n|M|s - n \rangle = \\ &= \mathcal{N}(s) \left[\exp \left(-\frac{\left((m - n) - c[s] \right)^2}{k[s]} \right) + \exp \left(-\frac{\left((m - n) + c[s] \right)^2}{k[s]} \right) \right] \end{aligned} \quad (32)$$

where: $c[s]$ is (close to) zero for $s < s^b$ and (almost) linear for $s > s^b$:

$$c[s] \approx \max[0, c_0(s - s^b)] \quad (33)$$

This type of parametrization fits the measured data quite well (the red line in Fig. 12) and is convenient for our further analysis. We will call s^b the **bifurcation point**. For our generic data ($K_0 = 2.2$, $\Delta = 0$ and $K_4 = 0.943$) the best fits yield: $s^b = 2020$ and $c_0 = 0.31$.

Another phenomenological parametrization which fits the data around bifurcation point even better (yellow curve in Fig. 12) is:

$$c[s] = c_0 s \exp(-s^b/s) \quad (34)$$

It is consistent with (33) for small and large s (compared to s^b). We will return to this parametrization when analyzing the phase transitions in the next sections.

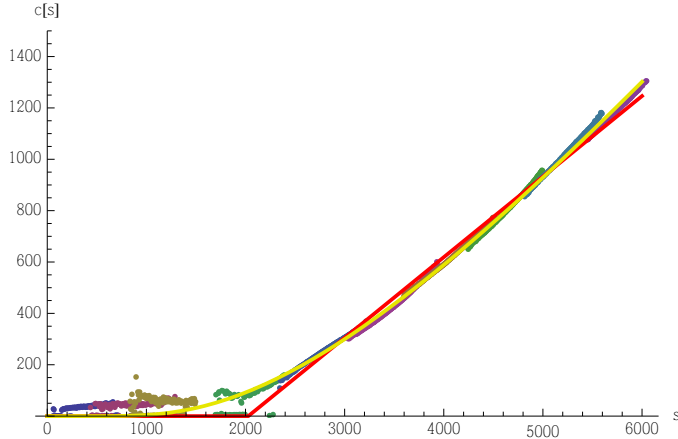


Figure 12: The bifurcation shift $c[s]$ measured in phase 'B' (for $K_0 = 2.2$, $\Delta = 0.0$ and $K_4 = 0.943$) together with the best fits using eq. (33) (red line) and (34) (yellow line).

The last function that should be fitted is $k[s]$ which is very well approximated by a linear function, independently of whether we are below or above the bifurcation point (Fig. 13). The behavior is consequently the same as in phase 'C' (21):

$$k[s] = \Gamma(s - 2n_0) \quad (35)$$

The best fit yields: $\Gamma = 36.8$, $n_0 = 5.4$ which is of the same order as the values measured in the de Sitter phase 'C'.

As we are interested in properties of the transfer matrix in the large volume limit (where critical values of K_4 are much higher) it is important to check how the results depend on K_4 . The plots of $c[s]$ and $k[s]$ for different K_4 are presented in Fig. 14. In general, the functional form (32)-(35) is adequate for different values of K_4 . With regards to the parameters entering in (32)-(35), the change of K_4 does not influence the position of bifurcation point s^b while bifurcation slope c_0 and effective Newton constant Γ rise when K_4 is increased.

Let us use these results to explain (at least qualitatively) the behavior of the system in phase 'B'. In our 'full CDT' simulations (with $t_{tot} = 80$) we analyze systems with large total volume ($\geq 40k$ simplices) for which K_4 is big. As a result c_0 and consequently $c[s]$ are large in the interesting region ($s > s^b$). Naively

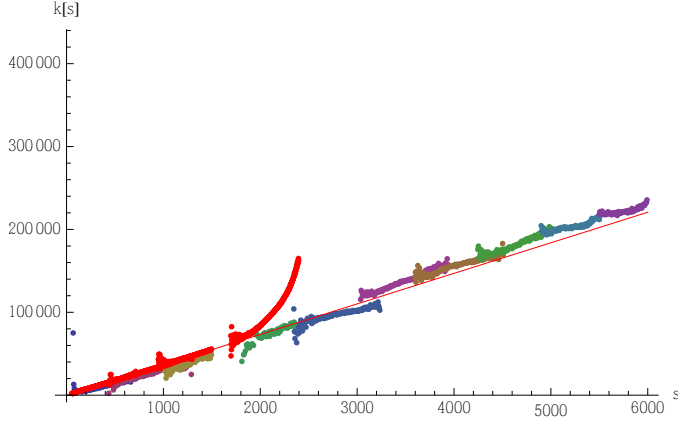


Figure 13: The kinetic coefficient $k[s]$ measured in phase 'B' (for $K_0 = 2.2$, $\Delta = 0.0$ and $K_4 = 0.943$). The red points correspond to the fit of the single Gaussian (which is not valid after crossing bifurcation point (for $s = n+m > s^b$)). Different colors correspond to the fit of double Gaussian (32) which is reliable also above bifurcation point (for $s > s^b$). The bifurcation point s^b can be identified as the point at which the fit of the single Gaussian starts to diverge from a linear behavior. It is consistent with the direct measurement of s^b (see Figure 12).

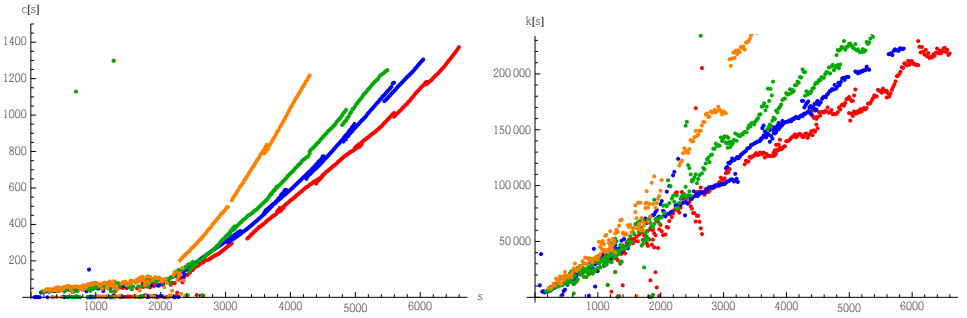


Figure 14: The bifurcation shift $c[s]$ (left) and the kinetic coefficient $k[s]$ (right) measured in phase 'B' ($K_0 = 2.2$, $\Delta = 0.0$) for different values of $K_4 = 0.933$ (red), 0.943 (blue), 0.953 (green), 0.973 (orange). The bifurcation point s^b is stable whereas the slope of the shift c_0 and the value of Γ rise as K_4 is increased.

speaking, configurations with very large difference of spatial volume in the adjacent time slices should be favored (most probable $(m - n)$ is large) and a kind of 'anti-ferromagnetic' behavior with ...-'large'-'small'-'large'-'small'-'.... volume distribution should be observed. This is exactly what we see in CDT systems with small time periods $t_{tot} = 2, 4, 6$ used in the transfer matrix measurements, but for $t_{tot} = 80$ the observed behavior is very different and the volume distribution is 'collapsed' to just one time slice. In order to explain this phenomena

we must take into account the entropic factor (the potential part in the transfer matrix 'language'). Due to strong dependence of K_4 on the total volume the exact measurement of the potential in the large volume range is beyond our reach at the moment. Instead let us present a theoretical model in which the potential is exactly the same as in phase 'C' (20). For simplicity we will consider only the leading behavior setting $\lambda, \delta, n_0 = 0$. Consequently:

$$\langle n|M|m \rangle = \exp\left(-\frac{\mu}{\Gamma}\left(\frac{n+m}{2}\right)^{1/3}\right) \left[\exp\left(-\frac{\left((m-n) - [c_0(n+m-s^b)]_+\right)^2}{\Gamma(n+m)}\right) + \exp\left(-\frac{\left((m-n) + [c_0(n+m-s^b)]_+\right)^2}{\Gamma(n+m)}\right) \right] \quad (36)$$

where: $[\cdot]_+ = \max(\cdot, 0)$.

Now we can perform the same kind of 'effective' Monte Carlo simulations as explained in section 3 in which the theoretical transfer matrix (36) will be used to generate volume distributions $\{n_t, t = 1..t_{tot}\}$ with the probability given by eq. (18). We choose the parameters of our model to be the values measured in the real 'full CDT' simulations: $\Gamma = 37, \mu = 15, s^b = 2000$ and $c_0 = 0.1 - 0.3$. The resulting volume distribution for small and large t_{tot} is presented in Fig. 15. As a reference case we also plot volume distribution for $c_0 = 0$ for which we recover the generic behavior found in the de Sitter phase 'C'.

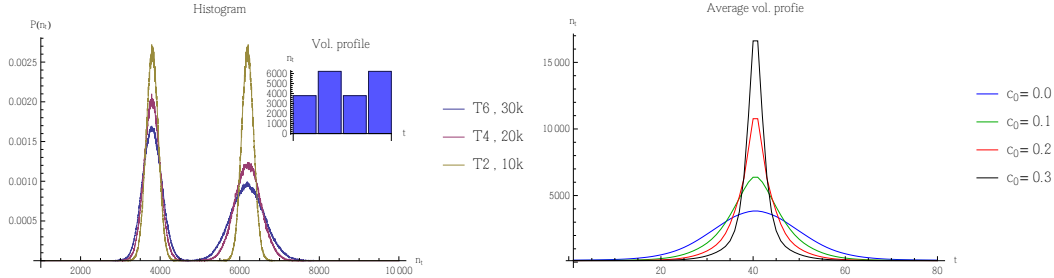


Figure 15: Left: the histogram of the spatial volume distributions measured in the effective Monte Carlo model (36) for $c_0 = 0.3$ and $t_{tot} = 2, 4, 6$. The two Gaussian peaks correspond to odd and even time slices respectively. As a result the average volume profile is 'anti-ferromagnetic' with quantum fluctuations around: ...-3.8k-6.2k-3.8k-6.2k-.... Right: the average spatial volume measured in the same model for $t_{tot} = 80, \bar{N}_{41} = 100k$ and different values of c_0 . The shape of the volume profile is consistent with the 'collapsed' blob structure.

For small t_{tot} the expected 'anti-ferromagnetic' structure is observed, while for large t_{tot} a single 'collapsed' blob forms. The strength of the 'collapsed' behavior depends on c_0 . This simple model explains very well (at least at a qualitative level) the volume distribution inside phase 'B'. In reality we should take into account that the value of c_0 appropriate for large K_4 used in 'full CDT' simulations is probably much bigger (leading to a much more narrow distribution for large t_{tot}). Also the real entropic / potential part may support a 'narrowing' of the volume distribution.

7 Phase transitions

When one applies the conventional methods to analyze the phase transitions observed in four-dimensional CDT one obtains strong evidence that the 'A'-'C' transition is a first order transition while the 'B'-'C' transition is a second (or higher) order transition [15]. These results are based on the analysis of order parameters defined as variables conjugate to bare coupling constants in the Regge action (2). By looking at the susceptibility of the order parameters one can identify the position of the phase transition lines in phase diagram (Fig. 16). At the same time the critical exponents, scaling properties and large volume behavior enable one to analyze the order of the phase transition. The order parameters in question reflect some global characteristics of the CDT triangulations (e.g. the ratio $N_0/N^{\{4,1\}}$). A change in such order parameters does not necessarily give much insight into the 'microscopic' nature of the phase transitions, which is an obvious drawback of this approach, in particular if one wants to find algorithms which can beat the critical slowing down observed near the transitions.

We will try to use the transfer matrix to obtain additional information about the phase transitions.

The 'A'-'C' phase transition is easily visible in the transfer matrix kinetic part. When we approach the phase transition line from phase 'C' (by increasing K_0 and keeping Δ fixed) the kinetic part of the minisuperspace effective action (15) smoothly vanishes. Near an 'A'-'C' phase transition point the cross-diagonals of the measured transfer matrix are almost flat. Just after the phase transition we can observe the formation of the 'artificial' anti-Gaussian term discussed in detail in section 4. For $\Delta = 0.6$ the phase transition point can be identified at $K_0 = 4.75 \pm 0.05$ (see Fig. 17) which is fully consistent with the location found using the 'traditional' approach used in [15].

The 'B'-'C' phase transition is not as easily visible. In the previous section we parametrized the kinetic part of the transfer matrix in phase 'B' by a sum of two Gaussians (32)-(35). An obvious parameter to look at is the bifurcation point s^b . For small volumes $s = n + m < s^b$ the kinetic part is the same as in

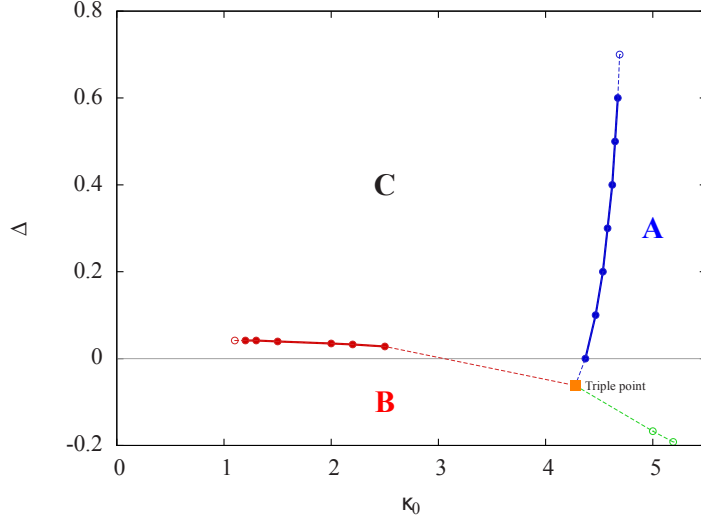


Figure 16: The CDT phase diagram measured by 'traditional' methods based on the order parameters analysis.

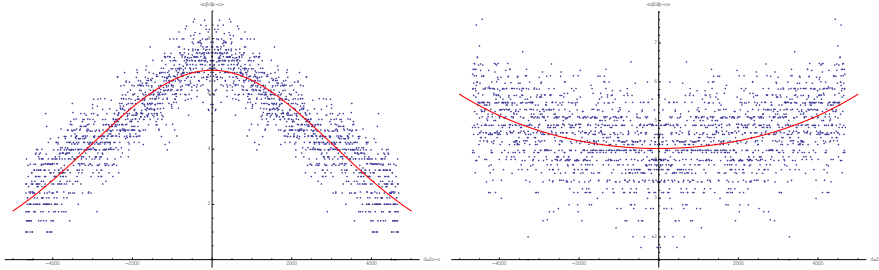


Figure 17: The cross-diagonal elements of the transfer matrix for $s = n + m = 5000$ measured for $\Delta = 0.6$. The left chart presents data for $K_0 = 4.7$ (phase 'C') while the right chart presents the data for $K_0 = 4.8$ (phase 'A'). The change of the behavior is clearly visible, which enables us to identify the phase transition point.

phase 'C'. The difference, responsible for the 'collapsed' behavior in phase 'B', is observed for large volumes $s > s^b$. Thus it is a natural conjecture that the 'B'-'C' phase transition is related to the appearance of a bifurcation point s^b . However, as we will see that is not the case. If we start in phase 'B', keep K_0 fixed and increase Δ in order to cross the 'B'-'C' phase transition line the value of s^b also increases. Thus it is natural to treat the condition $s^b \rightarrow \infty$ as a sign of a phase transition. In Figure 18 we present the plot of $1/s^b$ as a function of Δ for $K_0 = 2.2$. Different colors correspond to two methods of measuring s^b . The relation seems to be linear, implying the transition to occur for $\Delta = 0.2 - 0.3$. This value of Δ is much higher than critical value measured with the 'traditional' approach

($\Delta \approx 0.05$). Using s^b as an indicator of a phase transition we are seemingly observing something different from the formerly observed 'B'-'C' transition. We will discuss this in the next section.

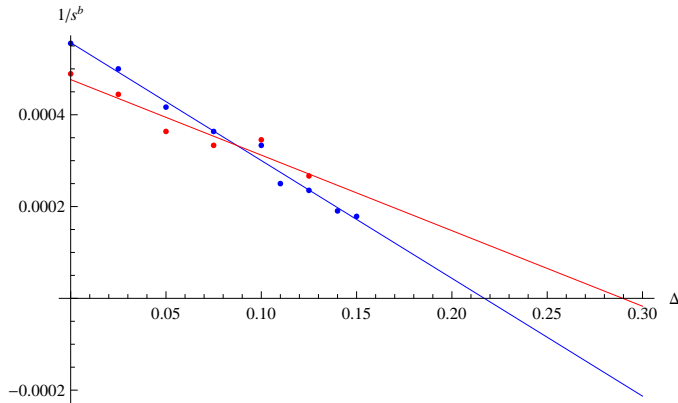


Figure 18: The (inverse of) bifurcation point s^b as a function of Δ (for fixed $K_0 = 2.2$). Colors correspond to two different ways of measurement: direct (red points) and indirect (blue points) - see footnote ³.

8 A new 'bifurcation' phase ?

In the previous section we provided evidence that the 'B'-'C' phase transition defined by the transfer matrix kinetic term change (bifurcation) is observed for the values of Δ much higher than in the 'traditional' analysis using as order parameter(s) the variables conjugate to the coupling constants. This result is based on the interpolation of the (inverse of) bifurcation point as a function of Δ . One may argue that this relation may change in the vicinity of transition moving the 'critical' Δ lower. However, it is possible to directly observe the 'bifurcation' structure also for $0.1 < \Delta < 0.3$ if one uses a total volume \bar{N}_{41} large enough (see Figure 19) and performs the simulations with small t_{tot} . At the same time the average volume profile for large t_{tot} has a shape characteristic for the de Sitter phase. In fact, if one looks at the transfer matrix data nothing special happens while crossing the 'B'-'C' phase transition line ($\Delta \approx 0.05$ for $K_0 = 2.2$).

³Red points correspond to s^b measured directly by fitting eq. (33) to the measured data. This method requires performing transfer matrix measurements also in the region of volumes much higher than s^b which is difficult as we approach phase transition point. Blue points correspond to the indirect method based on identifying a point at which the single Gaussian does no longer fit measured cross-diagonals - recall Fig. 13 for details. The larger the Δ the more difficult it is to observe the shift away from a single-Gaussian distribution. Therefore the values of $1/s^b$ for large Δ are probably underestimated when using this second method.

This is in obvious contradiction with the 'traditional' phase diagram presented in Fig. 16.

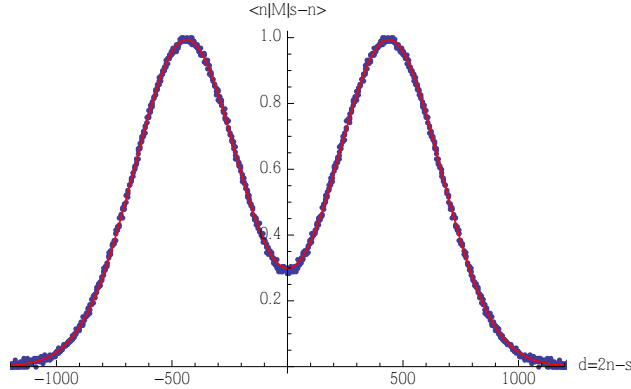


Figure 19: The cross diagonal elements of the transfer matrix measured for $K_0 = 2.2$ and $\Delta = 0.125$ which according to the 'traditional' approach lies well inside the de Sitter phase 'C'. Data are measured for $s = n + m = 15000$. The double-Gaussian bifurcation structure characteristic for phase 'B' is still clearly visible.

To explain this phenomenon we refer back to Figure 15 (right) in which the average volume profile in the effective Monte Carlo model with 'bifurcated' transfer matrix (36) is presented. For small bifurcation slopes (c_0) the volume profile is practically identical with that of the generic de Sitter phase even in systems with large total volumes ($\bar{N}_{41} = 100k$). For medium bifurcation slopes the volume profile gets narrower (in the time direction) but the general shape does not change much. Only for large c_0 the volume profile is substantially 'collapsed'.

If one plots the average volume profiles measured in 'full CDT' for $K_0 = 2.2$ and different values of $\Delta = 0.0 - 0.6$ (Fig. 20) the result looks qualitatively the same. For $\Delta \geq 0.4$ the shape is almost indifferent and then starts 'narrowing' for $0.1 \leq \Delta \leq 0.3$ to finally 'collapse' to the generic phase 'B' for $\Delta = 0.0$.

To justify this picture we measured the bifurcation structure for $0.1 \leq \Delta \leq 0.3$. It required going into large total volumes which substantially increased simulation time. To get better statistics we focused just on selected cross-diagonals of the measured transfer matrix by choosing the global volume fixing term (13) very peaked at $n_{vol} = 20k, 40k, 60k, 80k, \dots$ and performing measurement only if $n + m = n_{vol}$. We fitted the double-Gaussian (32) to the measured cross-diagonals and extracted the bifurcation shift $c[n_{vol}]$. Finally we used the parametrization (34) (which seems to better reproduce our data) to calculate the values of the bifurcation point s^b and the slope c_0 . We present these results in Fig. 21. As expected the bifurcation slope c_0 gradually grows when Δ is decreased which results in the observed 'narrowing' of the spatial volume distribution. Probably

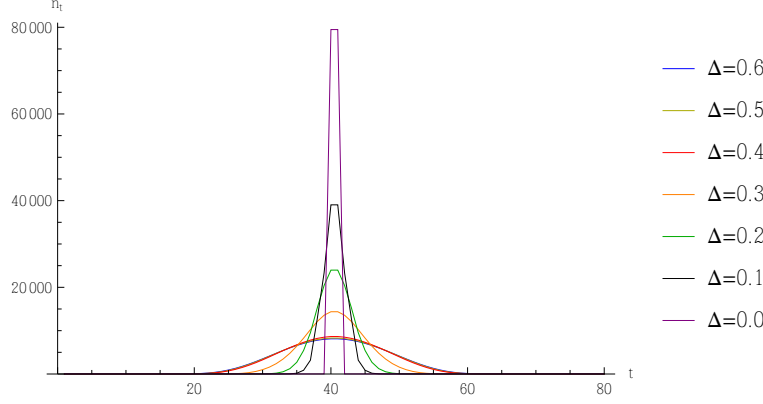


Figure 20: The average spatial volume profiles measured in 'full CDT' for $K_0 = 2.2$ and $t_{tot} = 80$ ($\bar{N}_{41} = 160k$).

other components of the micro-structure (which our transfer matrix model does not take into account) also change smoothly to finally 'collapse' showing the traditional 'B'-'C' phase transition. As a result the 'traditional' order parameters are insensitive to bifurcation kind of transition around $\Delta = 0.3$.

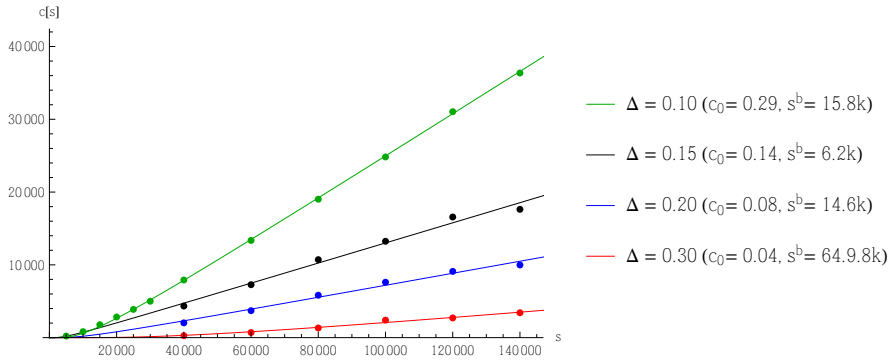


Figure 21: The bifurcation shifts measured for $K_0 = 2.2$ and different values of Δ (dots) and the best fits of $c[s] = c_0 \exp(-s^b/s)s$ (lines).

Summarizing, we conclude that a previously undiscovered '**bifurcation**' phase may exist in four-dimensional CDT. This phase should lie between 'B' and 'C' phases. Its generic 3-volume (temporal) distributions measured in 'full-CDT' (large t_{tot}) has a blob structure resembling that of the phase 'C', but there seem to be important differences. As an example we present the spatial volume distributions for different total volumes (\bar{N}_{41}) measured inside the new phase for $K_0 = 2.2$ and $\Delta = 0.125$ (Fig. 22). The volume distributions were rescaled both in time ($\tau = t/\bar{N}_{41}^{1/d_H}$) and space ($n(\tau) = n_t/\bar{N}_{41}^{1-1/d_H}$) with $d_H = 4$. In generic

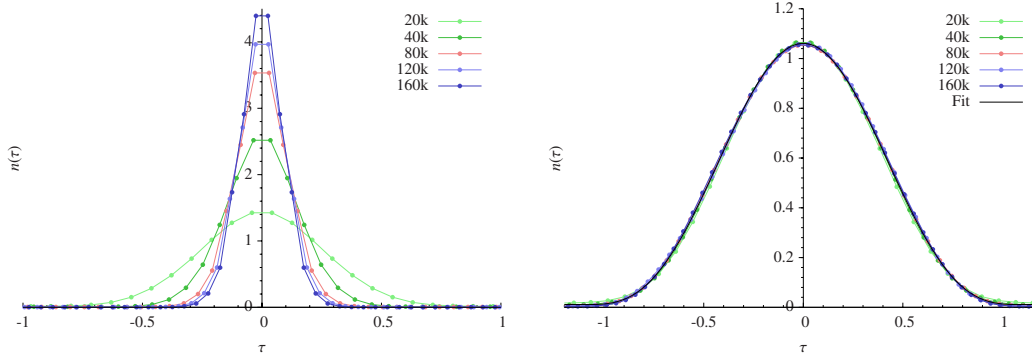


Figure 22: The full CDT (temporal) volume distributions measured inside the perspective 'bifurcation' phase for $K_0 = 2.2$, $\Delta = 0.125$ (left) and inside the de Sitter phase 'C' for $K_0 = 2.2$, $\Delta = 0.6$ (right). Different colors correspond to different total volumes \bar{N}_{41} . The data were rescaled to fit a single curve if Hausdorff dimension was 4. The lack of appropriate scaling in the new phase is an important difference compared to the generic phase 'C'.

phase 'C' ($\Delta = 0.6$) the Hausdorff dimension $d_H = 4$ and the rescaled volume distributions fall into one universal curve. The scaling for $\Delta = 0.125$ is evidently different. This is a strong argument in favor of the existence of a genuine new phase. In fact the scaling of volume profiles in the bifurcation region tends to $d_H = \infty$ for large volumes which is surprisingly consistent with our effective transfer matrix model (36) and characteristic for the generic phase 'B' - see Fig. 23. However, there is also no reason to doubt that the 'traditional' 'B'-'C' transition is still there, so seemingly we discovered a new phase separating the 'old' phase 'C' and phase 'B'.

9 Summary and conclusions

The recently introduced effective transfer matrix labeled only by the spatial volume provides an interesting tool for analyzing Causal Dynamical Triangulations in four dimensions. Using full 4D CDT simulations and the factorization (10), we have determined the effective transfer matrix. The effective Lagrangian

$$L_C(n, m) = \frac{1}{\Gamma} \left[\frac{(n-m)^2}{n+m-2n_0} + \mu \left(\frac{n+m}{2} \right)^{1/3} - \lambda \left(\frac{n+m}{2} \right) - \delta \left(\frac{n+m}{2} \right)^{-\rho} \right]$$

describes very well the measured transfer matrix in the de Sitter ('C') phase and can seemingly be used for large volumes.

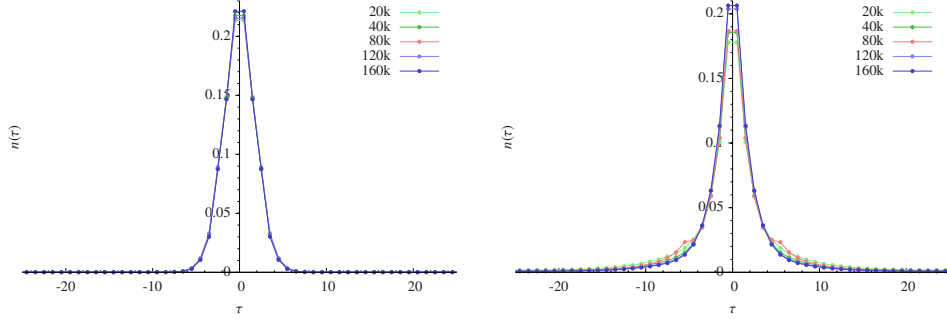


Figure 23: The full CDT (temporal) volume distributions measured inside the perspective 'bifurcation' phase for $K_0 = 2.2$, $\Delta = 0.125$ (left) and in the 'effective' Monte Carlo model (36) with bifurcation slope $c_0 = 0.3$ (right). Different colors correspond to different total volumes \bar{N}_{41} . The data were rescaled to fit a single curve for Hausdorff dimension $d_H = \infty$.

Assuming validity of decomposition (10) we introduced *an effective transfer matrix model* reducing the degrees of freedom only to spatial volumes, i.e. a model which neglects completely the internal structure of slices. The simplified model perfectly reproduced all results obtained so far using the full model of 4D Causal Dynamical Triangulations.

Recent studies of a similar effective model [16] indicated that the whole phase structure of CDT can be explained by the minisuperspace action (4) if we allow for infinite and/or negative values of the effective action parameters. Therefore we extended our analysis of the effective transfer matrix / action to the other CDT phases to check whether this simple scenario is realized. It turns out that reality is more complicated.

We provided strong evidence that inside the 'uncorrelated' phase 'A' the effective Lagrangian takes the form

$$L_A(n, m) = \mu(n^\alpha + m^\alpha) - \lambda(n + m)$$

with $\alpha \neq 1/3$. The absence of a kinetic term can be interpreted as a causal disconnection of different time slices, i.e. the phenomenon of 'asymptotic silence' observed both in classical and quantum approaches to gravity in the regime of extreme curvatures / energy densities [17]. In this context the 'uncorrelated' phase might gain some physical meaning.

The situation is more difficult in the 'collapsed' phase 'B'. Inside this phase the transfer matrix can be parametrized as follows:

$$\langle n | M_B | m \rangle = \mathcal{N}[n + m] \left[\exp \left(- \frac{\left((m - n) - [c_0(n + m - s^b)]_+ \right)^2}{\Gamma(n + m - 2n_0)} \right) + \right.$$

$$+ \exp \left(- \frac{\left((m-n) + [c_0(n+m-s^b)]_+ \right)^2}{\Gamma(n+m-2n_0)} \right) \Bigg]$$

where: $[\cdot]_+ = \max(\cdot, 0)$. The properties of the spatial volume distribution depend strongly on the parameter c_0 , while the phase transition to the de Sitter phase 'C' is connected with the $s^b \rightarrow \infty$ limit. We showed by direct measurement that this kind of phase transition occurs for the Δ coupling constant much higher than indicated by the previous phase transition studies and it points to a new 'bifurcation phase' separating the 'B' and 'C' phases. That such a putative phase is not an artifact of the effective transfer matrix model is supported by measurements performed in the full CDT theory, which show that the scaling of the spatial volume distribution as a function of the total four-volume indeed is different close the 'old' 'B'-'C' transition than it is deep into phase 'C' where the Hausdorff dimension $d_H = 4$. The exact nature of this new phase deserves further studies.

10 Acknowledgments

JG-S acknowledges the Polish National Science Centre (NCN) support via the grant DEC-2012/05/N/ST2/02698. JA and AG were supported by the ERC-Advance grant 291092, "Exploring the Quantum Universe" (EQU). JA acknowledges support of FNU, the Free Danish Research Council, from the grant "quantum gravity and the role of black holes".

References

- [1] T. Regge: *General relativity without coordinates*, Nuovo Cim. 19 (1961) 558.
- [2] F. David, *Planar Diagrams: Two-Dimensional Lattice Gravity and Surface Models*, Nucl. Phys. B257 (1985) 45.
V. A. Kazakov, A. A. Migdal, I. K. Kostov, *Critical Properties of Randomly Triangulated Planar Random Surfaces*, Phys. Lett. B157 (1985) 295-300.
- J. Ambjorn, B. Durhuus and J. Frohlich, *Diseases of Triangulated Random Surface Models, and Possible Cures*, Nucl. Phys. B **257** (1985) 433.
- J. Ambjorn, B. Durhuus, J. Frohlich and P. Orland, *The Appearance of Critical Dimensions in Regulated String Theories*, Nucl. Phys. B **270** (1986) 457.

- D.V. Boulatov, V.A. Kazakov, I.K. Kostov and A.A. Migdal, *Analytical and numerical study of the model of dynamically triangulated random surfaces*, Nucl. Phys. B 275 (1986) 641-686.
- [3] V. G. Knizhnik, A. M. Polyakov and A. B. Zamolodchikov, *Fractal Structure of 2D Quantum Gravity*, Mod. Phys. Lett. A 3 (1988) 819.
 F. David, *Conformal Field Theories Coupled to 2D Gravity in the Conformal Gauge*, Mod. Phys. Lett. A 3 (1988) 1651.
 J. Distler and H. Kawai, *Conformal Field Theory and 2D Quantum Gravity Or Who's Afraid of Joseph Liouville?*, Nucl. Phys. B **321** (1989) 509.
 J. Ambjørn and K.N. Anagnostopoulos: *Quantum geometry of 2D gravity coupled to unitary matter*, Nucl. Phys. B 497 (1997) 445-478 [hep-lat/9701006].
- [4] J. Ambjørn, S. Varsted: *Entropy estimate in three-dimensional simplicial quantum gravity*, Phys. Lett. B266 (1991) 285-290.
 M. E. Agishtein, A. A. Migdal: *Three-dimensional quantum gravity as dynamical triangulation*, Mod. Phys. Lett. A6 (1991) 1863-1884.
 D. V. Boulatov, A. Krzywicki: *On the phase diagram of three-dimensional simplicial quantum gravity*, Mod. Phys. Lett. A6 (1991) 3005-3014.
 J. Ambjørn, D. V. Boulatov, A. Krzywicki, S. Varsted: *The Vacuum in three-dimensional simplicial quantum gravity*, Phys. Lett. B276 (1992) 432-436.
 J. Ambjørn, S. Varsted: *Three-dimensional simplicial quantum gravity*, Nucl. Phys. B373 (1992) 557-580.
- [5] J. Ambjørn and J. Jurkiewicz: *Four-dimensional simplicial quantum gravity*, Phys. Lett. B 278 (1992) 42-50.
 M.E. Agishtein and A.A. Migdal: *Simulations of four-dimensional simplicial quantum gravity*, Mod. Phys. Lett. A 7 (1992) 1039-1062.
 S. Bilke, Z. Burda, A. Krzywicki, B. Petersson, J. Tabaczek and G. Thorleifsson: *4-D simplicial quantum gravity interacting with gauge matter fields*, Phys. Lett. B 418 (1998) 266; [hep-lat/9710077].
 S. Bilke, Z. Burda, A. Krzywicki, B. Petersson, J. Tabaczek and G. Thorleifsson: *4-D simplicial quantum gravity: Matter fields and the corresponding effective action*, Phys. Lett. B 432 (1998) 279 [hep-lat/9804011].
 J. Ambjørn, K. N. Anagnostopoulos and J. Jurkiewicz: *Abelian gauge fields coupled to simplicial quantum gravity*, JHEP 9908 (1999) 016 [hep-lat/9907027].

- S. Horata, H. S. Egawa, N. Tsuda, T. Yukawa: *Phase structure of four-dimensional simplicial quantum gravity with a $U(1)$ gauge field*, Prog. Theor. Phys. 106 (2001) 1037-1050. [hep-lat/0004021].
- [6] P. Bialas, Z. Burda, A. Krzywicki, B. Petersson: *Focusing on the fixed point of 4-D simplicial gravity*, Nucl. Phys. B472 (1996) 293-308. [hep-lat/9601024].
- B.V. de Bakker: *Further evidence that the transition of 4D dynamical triangulation is 1st order*, Phys. Lett. B 389 (1996) 238-242 [hep-lat/9603024].
- S. Catterall, R. Renken, J. B. Kogut: *Singular structure in 4-D simplicial gravity*, Phys. Lett. B416 (1998) 274-280. [hep-lat/9709007].
- [7] J. Ambjørn and R. Loll: *Non-perturbative Lorentzian quantum gravity, causality and topology change*, Nucl. Phys. B 536 (1998) 407-434 [hep-th/9805108].
- J. Ambjørn, J. Jurkiewicz and R. Loll: *A non-perturbative Lorentzian path integral for gravity*, Phys. Rev. Lett. **85** (2000) 924, [hep-th/0002050].
- J. Ambjørn, J. Jurkiewicz and R. Loll: *Non-perturbative 3d Lorentzian quantum gravity*, Phys. Rev. D **64** (2001) 044011 [hep-th/0011276].
- J. Ambjørn, J. Jurkiewicz and R. Loll: *Dynamically triangulating Lorentzian quantum gravity*, Nucl. Phys. B 610 (2001) 347-382 [hep-th/0105267].
- [8] J. Ambjørn, A. Goerlich, J. Jurkiewicz and R. Loll, *Nonperturbative Quantum Gravity*, Phys. Rept. **519** (2012) 127 [arXiv:1203.3591 [hep-th]].
- J. Ambjørn, J. Jurkiewicz and R. Loll: *Quantum gravity as sum over spacetimes*, Lect. Notes Phys. **807** (2010) 59-124, [gr-qc/0906.3947].
- J. Ambjørn, A. Görlich, J. Jurkiewicz, R. Loll: *CDT-an Entropic Theory of Quantum Gravity*, [hep-th/1007.2560].
- [9] J. Ambjørn, J. Jurkiewicz and R. Loll: *The universe from scratch*, Contemp. Phys. 47 (2006) 103-117 [hep-th/0509010].
- R. Loll: *The emergence of spacetime, or, quantum gravity on your desktop*, Class. Quant. Grav. 25 (2008) 114006 [gr-qc/0711.0273].
- [10] J. Ambjørn, J. Jurkiewicz and R. Loll: *Reconstructing the universe*, Phys. Rev. D 72 (2005) 064014 [hep-th/0505154].
- J. Ambjørn, A. Görlich, S. Jordan, J. Jurkiewicz and R. Loll: *CDT meets Horava-Lifshitz gravity*, Phys. Lett. B 690 (2010) 413-419 [hep-th/1002.3298].

- [11] J. Ambjørn, J. Jurkiewicz and R. Loll: *Emergence of a 4D world from causal quantum gravity*, Phys. Rev. Lett. **93** (2004) 131301, 4 pages [hep-th/0404156].
- J. Ambjørn, J. Jurkiewicz and R. Loll: *Semiclassical universe from first principles*, Phys. Lett. B **607** (2005) 205-213 [hep-th/0411152].
- J. Ambjørn, J. Jurkiewicz and R. Loll: *Reconstructing the universe*, Phys. Rev. D **72** (2005) 064014, 24 pages [hep-th/0505154].
- J. Ambjørn, A. Görlich, J. Jurkiewicz and R. Loll: *Planckian birth of the quantum de Sitter universe*, Phys. Rev. Lett. **100** (2008) 091304, 4 pages [hep-th/0712.2485].
- J. Ambjørn, J. Jurkiewicz and R. Loll: *The self-organized de Sitter universe* [gr-qc/0806.0397].
- J. Ambjørn, A. Görlich, J. Jurkiewicz and R. Loll: *Geometry of the quantum universe*, Phys. Lett. B **690** (2010) 420-426 [hep-th/1001.4581].
- [12] J. Ambjørn, A. Görlich, J. Jurkiewicz and R. Loll: *The nonperturbative quantum de Sitter universe*, Phys. Rev. D **78** (2008) 063544, 17 pages [hep-th/0807.4481].
- [13] J. Ambjørn, A. Görlich, J. Jurkiewicz, R. Loll, J. Gizbert-Studnicki, T. Trzesniewski: *The semiclassical limit of causal dynamical triangulations*, Nucl. Phys. B **849** (2011) 144-165 [hep-th/1102.3929].
- [14] J. Ambjørn, J. Gizbert-Studnicki, A.T. Görlich, J. Jurkiewicz: *The transfer matrix in four-dimensional CDT*, JHEP **09** (2012) 017 [hep-th/1205.3791].
- [15] J. Ambjørn, S. Jordan, J. Jurkiewicz, R. Loll: *A second-order phase transition in CDT*, Phys. Rev. Lett. **107**, 211303 (2011) [hep-th/1108.3932].
- J. Ambjørn, S. Jordan, J. Jurkiewicz, R. Loll: *Second- and First-Order Phase Transitions in CDT*, Phys. Rev. D **85**, 124044 (2012) [hep-th/1205.1229].
- [16] L. Bogacz, Z. Burda, B. Waclaw: *Quantum widening of CDT universe*, Phys. Rev. D **86**, 104015 (2012) [hep-th/1204.1356]
- [17] J. Mielczarek: *Asymptotic silence in loop quantum cosmology*, AIP Conference Proceedings;Feb2013, Vol. 1514 Issue 1, p81 [gr-qc/1212.3527]